

Response of reinforced concrete piles including soil–pile interaction effects

Suchart Limkatanyu^{a,*}, Kittisak Kuntiyawichai^b, Enrico Spacone^{c,1}

^a Department of Civil Engineering, Faculty of Engineering, Prince of Songkla University, Songkhla, 90110, Thailand

^b Department of Civil Engineering, Faculty of Engineering, Ubonratchathani University, Ubonratchathani, 34190, Thailand

^c Department of PRICOS, Faculty of Architecture, University "G. D'Annunzio", 65127 Pescara, Italy

ARTICLE INFO

Article history:

Received 29 June 2008

Received in revised form

24 February 2009

Accepted 3 March 2009

Available online 5 April 2009

Keywords:

Soil–structure interaction

Reinforced concrete

Foundation piles

Fiber model

Cyclic loads

Finite element method

Nonlinear frame analysis

Simulation

ABSTRACT

This paper discusses the importance of modeling soil–pile interaction in the response of reinforced concrete (RC) piles. A displacement-based, RC beam–column fiber model with distributed lateral deformable supports is presented first. The formulation is general and applies to both monotonic and cyclic loads. The proposed model is simple, computationally efficient and capable of representing the salient features of the soil–pile interaction, including dragging force and gap formation along the pile–soil interfaces as well as hysteretic responses of piles and surrounding soils. Two applications are presented to illustrate the model characteristics, to show the model capabilities, and to discuss the importance of modeling the pile–soil system. The first application deals with a single end-bearing pile embedded in a cohesionless soil. The proposed beam–column model is used to investigate the effects of different model parameters on the pile–soil response, including pile length, pile diameter, and pile and soil nonlinearities. The second application validates the accuracy of the proposed model with the experimental results of a cyclic test on a RC pile/shaft system where the influence of the pile–soil interaction is essential. Results from the correlation studies indicate that the proposed model can represent well both global and local responses of the pile–soil system. The effects of the interfacial characteristics between pile and soil on the system response are also studied.

© 2009 Elsevier Ltd. All rights reserved.

1. Introduction

Due to the increasing need for infrastructures and the decreasing availability of space, both structural and geotechnical engineers are challenged to design, analyze, and evaluate more expensive and strategic structural systems (e.g. high-rise buildings, offshore platforms, multi-story highways, etc.) for extreme lateral loadings (e.g. earthquakes, gusty winds, terrorist attacks, etc.). In weaker soils, foundation piles, both single pile and pile groups, may be used to transfer large superstructure loads through deeper soils. In these cases, the influence of the foundation piles should be included. Typically, seismic design codes (e.g. NEHRP-97 [1]) neglect the seismic behavior of the foundation piles, or they greatly simplify it, because the structural-period lengthening due to the foundation flexibility for most design spectra leads mainly to a reduction in seismic design forces. This is not always the case when near-fault ground motions (possibly containing long-period pulses) are considered or when the structural displacements rather

than the structural forces are the key design parameters, as in the case of the Displacement-Based Seismic Design Methodology [2,3]. Furthermore, damages of the pile foundations during recent destructive earthquakes (e.g. 1989 Loma Prieta Earthquake [4], 1995 Hyogoken-Nambu Earthquake [5,6], etc.) are reminders of the importance of the foundation piles and of their influence on the overall structural response. Consequently, the inclusion of the soil–pile system into the foundation numerical model may be important for design, analysis, and performance evaluation of structures under seismic actions. It is commonly accepted that foundation piles should remain elastic under seismic loadings in order to avoid difficult subsurface inspections and expensive repairs of the damaged foundations. Nevertheless, the bending moment induced in the piles by the design seismic actions can be large enough to cause flexural damage in the piles, as shown by recent post-earthquake investigations [4–6]. The flexural damage in the piles can reduce both the foundation stiffness and its strength, hence affecting the serviceability and load-carrying capacity of the whole structure–foundation–soil system. Furthermore, the role of the foundation piles in the seismic rehabilitation of existing buildings is crucial. Seismic retrofit of existing buildings can be economically achieved by the adding steel bracing or RC shear walls. This can however result in severe seismic demands on the existing foundation piles.

* Corresponding author. Tel.: +66 74 287129; fax: +66 74 459396.

E-mail addresses: suchart.l@psu.ac.th (S. Limkatanyu), kittisak.ubu@gmail.com (K. Kuntiyawichai), e.spacone@unich.it (E. Spacone).

¹ Tel.: +39 085 4537276; fax: +39 085 4537255.

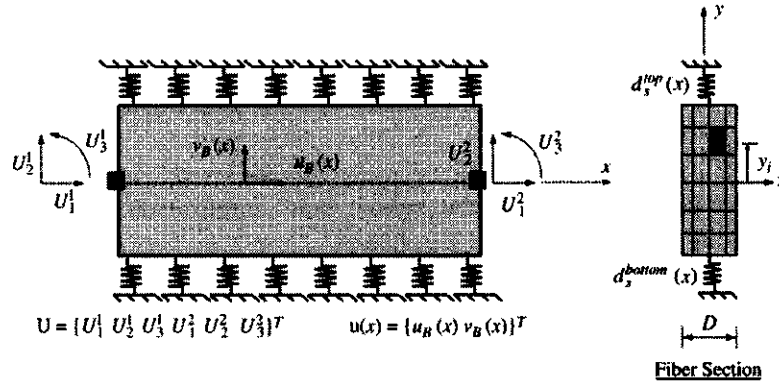


Fig. 1. 2-node displacement-based beam-column element with lateral deformable supports [16].

Thus far, several analytical models have been proposed in the published literature to study the soil-pile interaction problem. These models range from comparatively simple approaches in which the soils surrounding the pile are represented as a set of discrete springs, to sophisticated 3D finite element models. These analytical models are classified here into three categories: (a) elastic continuum models [7]; (b) solid (2D or 3D) finite element models [8–12]; (c) line (1D) beam-column elements based on beam theories [13–15]. The pros and cons of the aforementioned analytical models are summarized in Limkatanyu and Spacone [16]. The boundary element models have also been used to study the soil-pile interaction problem [17].

The main objectives of this paper are to present a newly developed pile-soil beam-column element, to study its main parameters, and to validate the proposed model through correlation studies of large-scale tests on piles subjected to lateral loadings. The formulation of the pile-soil beam-column element is based on the principle of virtual displacements. Other element formulations are presented elsewhere [16]. The *Winkler Foundation* model is employed to represent the surrounding soils (Winkler [18]). Two applications are presented to illustrate the model characteristics, to show the model capabilities, and to discuss the importance of modeling the pile-soil system. The first application investigates the effects of several model parameters on the lateral response of the pile-soil systems. The second application deals with the correlation studies of a large-scale RC pile/shaft experimental test. It is important to note that this study focuses only on the soil-pile interaction in firm non-liquefiable soils. The kinematic interaction due to scattering of the incoming seismic waves and the soil liquefaction effects are not included in this study.

2. Definitions

The 2-node displacement-based beam-column element with lateral deformable supports (e.g. soil) [16] is shown in Fig. 1. The proposed beam-column element with lateral deformable supports comprises two components: a 2-node beam-column, plus continuous lateral springs representing the surrounding deformable medium.

Using the notation of Fig. 1, the element nodal displacements are:

$$\mathbf{U} = \{\mathbf{U}^1 : \mathbf{U}^2\}^T \quad (1)$$

where \mathbf{U}^1 and \mathbf{U}^2 are arrays containing the displacements at nodes 1 and 2, respectively. The corresponding nodal forces are $\mathbf{P} = \{\mathbf{P}^1 : \mathbf{P}^2\}^T$.

The section displacements are grouped in the following array:

$$\mathbf{u}(x) = \{u_B(x) \ v_B(x)\}^T \quad (2)$$

where $u_B(x)$ and $v_B(x)$ represent the axial and transverse displacements, respectively.

The section deformations are grouped in the following array:

$$\mathbf{d}_B(x) = \{\varepsilon_B(x) \ \kappa_B(x)\}^T \quad (3)$$

where $\varepsilon_B(x)$ and $\kappa_B(x)$ are the axial strain and the curvature, respectively.

The beam-column formulation follows the Euler-Bernoulli beam theory. Based on the small deformation assumption, the section deformations are found through the compatibility relations $\varepsilon_B(x) = du_B/dx$ and $\kappa_B(x) = dv_B^2/dx^2$. In matrix notation:

$$\mathbf{d}_B(x) = \partial_B \mathbf{u}(x) \quad (4)$$

where ∂_B is the following differential operator:

$$\partial_B = \begin{bmatrix} \frac{d}{dx} & 0 \\ 0 & \frac{d^2}{dx^2} \end{bmatrix} \quad (5)$$

The corresponding section forces $\mathbf{D}_B(x)$ are:

$$\mathbf{D}_B(x) = \{N_B(x) \ M_B(x)\}^T \quad (6)$$

where $N_B(x)$ and $M_B(x)$ are the axial load and the bending moment, respectively.

The lateral deformations $\mathbf{d}_s(x)$ are defined by the following array:

$$\mathbf{d}_s(x) = \{d_s^{\text{top}}(x) \ d_s^{\text{bottom}}(x)\}^T \quad (7)$$

where $d_s^{\text{top}}(x)$ and $d_s^{\text{bottom}}(x)$ are the lateral deformations at the top and bottom faces, respectively. Based on the Winkler foundation theory, the lateral deformations are determined through the following compatibility relations:

$$\begin{aligned} d_s^{\text{top}}(x) &= v_B(x) \\ d_s^{\text{bottom}}(x) &= v_B(x). \end{aligned} \quad (8)$$

Though these displacements are equal in the present formulation, they are kept distinct to maintain generality. Eq. (8) can be expressed in the following matrix form:

$$\mathbf{d}_s(x) = \mathbf{T}_s \mathbf{u}(x) \quad (9)$$

where \mathbf{T}_s is a transformation matrix defined as:

$$\mathbf{T}_s = \begin{bmatrix} 0 & 1 \\ 0 & 1 \end{bmatrix} \quad (10)$$

Finally, the lateral forces $D_s^{\text{top}}(x)$ and $D_s^{\text{bottom}}(x)$ corresponding to the lateral-support deformations are grouped in the $\mathbf{D}_s(x)$ array:

$$\mathbf{D}_s(x) = \{D_s^{\text{top}}(x) \ D_s^{\text{bottom}}(x)\}^T \quad (11)$$

3. Model formulation

The element formulation is based on the principle of virtual displacements. The element displacements $u(x)$ are expressed as functions of the nodal displacements U through the shape functions $N_B(x)$:

$$u(x) = N_B(x)U. \quad (12)$$

$N_B(x)$ are well-known Hermitian polynomials that define a linear axial displacement field and a cubic lateral displacement field.

3.1. Compatibility

Compatibility is enforced in the strong form. Upon substitution of Eq. (12) into Eqs. (4) and (9), the section and lateral deformations are directly related to the nodal displacements U through the following equations:

$$\begin{aligned} d_B(x) &= B_B(x)U \\ d_s(x) &= B_s(x)U \end{aligned} \quad (13)$$

where $B_B(x) = \partial_B N_B(x)$ is the pile section deformation–displacement matrix and $B_s(x) = T_s N_B(x)$ is the soil deformation–displacement matrix.

3.2. Equilibrium

Element equilibrium is enforced in the weak form. Application of the principle of virtual displacements and substitution of Eq. (13) yield the following equation:

$$\int_L B_B^T(x) D_B(x) dx + \int_L B_s^T(x) D_s(x) dx = P. \quad (14)$$

The total internal forces are expressed as the sum of the initial section forces $D_B^0(x)$ and $D_s^0(x)$ plus the force increments $\Delta D_B(x) = k_B(x) \Delta d_B(x)$ and $\Delta D_s(x) = k_s(x) \Delta d_s(x)$. $k_B(x)$ is the beam section stiffness matrix and $k_s(x)$ is the matrix containing the lateral-support stiffness. Then:

$$\begin{aligned} \int_L B_B^T(x) [D_B^0(x) + k_B(x) B_B^T(x) \Delta U] dx \\ + \int_L B_s^T(x) [D_s^0(x) + k_s(x) B_s(x) \Delta U] dx = P. \end{aligned} \quad (15)$$

Eq. (15) is rearranged to obtain the following incremental form of the equilibrium:

$$K \Delta U = P - P^0 \quad (16)$$

where K is the element stiffness matrix and P is the element force array

$$K = K_B + K_s \quad (17)$$

$$P = P_B + P_s \quad (18)$$

$P^0 = P_B^0 + P_s^0$ is the array containing the element initial forces.

In Eq. (17), K_B is the beam–column contribution to the element stiffness, and K_s is the contribution of the lateral supports:

$$K_B = \int_L B_B^T(x) k_B(x) B_B(x) dx \quad (19)$$

$$K_s = \int_L B_s^T(x) k_s(x) B_s(x) dx.$$

Similarly, in Eq. (18), P_B is the beam–column contribution to the element forces, and P_s is the contribution of the lateral supports:

$$P_B = \int_L B_B^T(x) D_B(x) dx \quad (20)$$

$$P_s = \int_L B_s^T(x) D_s(x) dx.$$

3.3. Section model

The cross section is subdivided into fibers. The beam section forces $D_B(x)$ are

$$D_B(x) = \sum_{j=1}^{nfb} \begin{bmatrix} -y_j \sigma_j A_j & \sigma_j A_j \end{bmatrix}^T \quad (21)$$

where j represents the generic fiber and nfb is the number of fibers in the RC section. y_j , σ_j , and A_j are the distance from the reference axis x (Fig. 1), the stress, and the area, respectively, of fiber j of the beam–column section. Indicating with E_j the fiber modulus, the beam–column section stiffness $k_B(x)$ is

$$k_B(x) = \sum_{j=1}^{nfb} \begin{bmatrix} E_j A_j & -y_j E_j A_j \\ -y_j E_j A_j & y_j^2 E_j A_j \end{bmatrix}. \quad (22)$$

The lateral-support forces $D_s(x)$ are:

$$D_s(x) = \{\sigma_s^{\text{top}} D \quad \sigma_s^{\text{bottom}} D\}^T \quad (23)$$

where σ_s^{top} and σ_s^{bottom} are the lateral pressures at the top and bottom interfaces, respectively. D is the width of the beam–column section. The lateral-support stiffness matrix $k_s(x)$ is a diagonal matrix defined as:

$$k_s(x) = \begin{bmatrix} E_s^{\text{top}} D & 0 \\ 0 & E_s^{\text{bottom}} D \end{bmatrix}. \quad (24)$$

E_s^{top} and E_s^{bottom} are the moduli of the top and bottom lateral supports, respectively.

The hysteretic behaviors of the concrete and steel laws are schematically presented in Fig. 2. The Kent and Park [19] law is used for the concrete. The tensile branch of the concrete is not considered in the present study. The Menegotto and Pinto [20] law is used for the steel reinforcement. For the present study, the finite element program FEAP [21] is used to host the proposed element.

3.4. Monotonic and cyclic p – y curves of cohesionless soils

In this study, the soils surrounding a pile are modeled as 1D springs continuously distributed along the pile length. Only cohesionless soils are considered in this study. Based on the model proposed by Reese et al. [22], the ultimate soil lateral strength p_u can be computed as the lesser of the following two values:

$$\begin{aligned} p_u = \gamma z \left[D (K_p - K_a) + z (K_p - K_0) \sqrt{K_p} \tan \alpha \right. \\ \left. + z K_0 \sqrt{K_p} \left(\frac{1}{\cos \alpha} + 1 \right) \tan \phi' \sin \beta \right] \end{aligned} \quad (25)$$

$$p_u = \gamma z D (K_p^3 + K_0 K_p^2 \tan \phi' - K_0) \quad (26)$$

where $K_p = \tan^2 (45^\circ + \phi'/2)$ is the passive earth pressure coefficient; $K_a = \tan^2 (45^\circ - \phi'/2)$ is the active earth pressure coefficient; K_0 is the at-rest earth pressure coefficient; ϕ' is the effective internal friction angle; $\alpha = \phi'/2$ is the angle defining the failure wedge shape; $\beta = 45^\circ + \phi'/2$; γ is the soil effective unit weight; z is the depth from the ground surface; and D is the pile diameter. The typical value of the at-rest earth pressure coefficient K_0 is 0.4, as recommended by Reese and Van Impe [23]. Eq. (25) accounts for the wedge-type failure near the surface while Eq. (26) accounts for the plane-strain failure at great depths below the ground surface. The monotonic backbone p – y curves relating the soil deformation to the soil pressure are shown for various depths in Fig. 3. Each monotonic backbone p – y curve comprises three linear portions and one parabolic portion. The initial linear

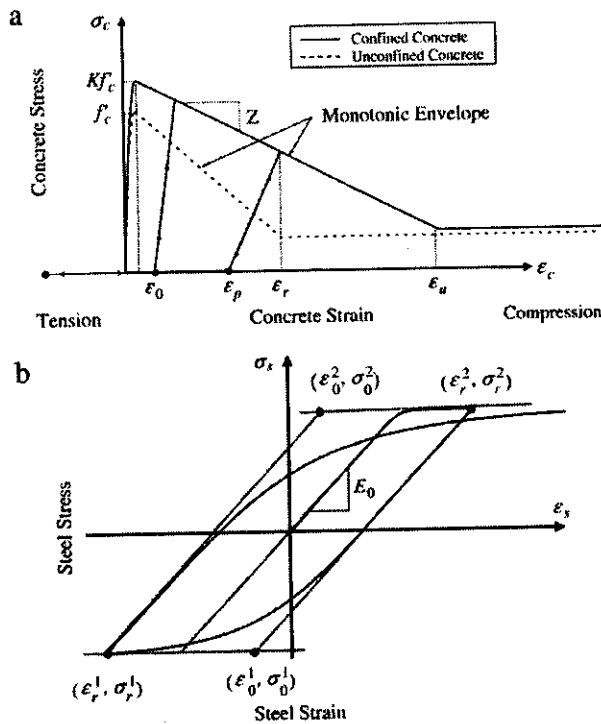


Fig. 2. Hysteretic uniaxial material models: (a) Concrete; (b) Steel reinforcement.

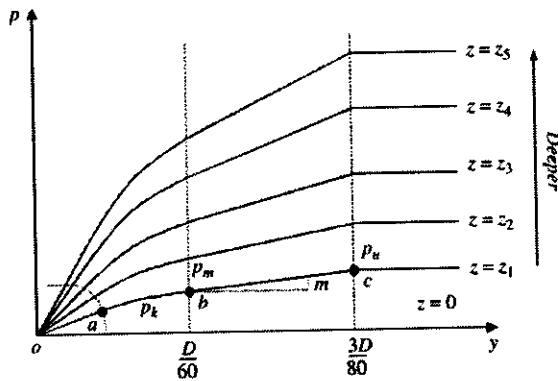


Fig. 3. Characteristic shape of p - y curves for sand (proposed by Reese et al. [22]).

portion (oa) represents the elastic behavior of the soil for small lateral deflections as suggested by Terzaghi [24]. The slope of this linear portion is equal to the product of the modulus subgrade n_h and the depth z measured from the surface. The recommended values of n_h can be found in Reese and Van Impe [23]. The flat-top portion (*beyond c*) represents the plastic behavior of the soil for large lateral deflections. These two linear portions are connected by a parabola (ab) and an inclined straight line (bc) in order to obtain a shape consistent with the experimental p - y curves [22]. It is noted that the deeper soils are stiffer and stronger than the shallower soils due to the high confining pressures.

The monotonic p - y curves of Fig. 3 serve as envelopes of the two cyclic p - y shown in Fig. 4. The model of Fig. 4(a) is elastic-perfectly plastic and ignores the gapping and dragging responses of the surrounding soil. The model of Fig. 4(b) takes into account the gapping and dragging responses observed during in situ tests on piles under lateral cyclic loadings (e.g. Brown et al. [25]). The hysteretic characteristics of the model developed by Arnold et al. [26] are modified for the proposed cyclic p - y model (Fig. 4(b)).

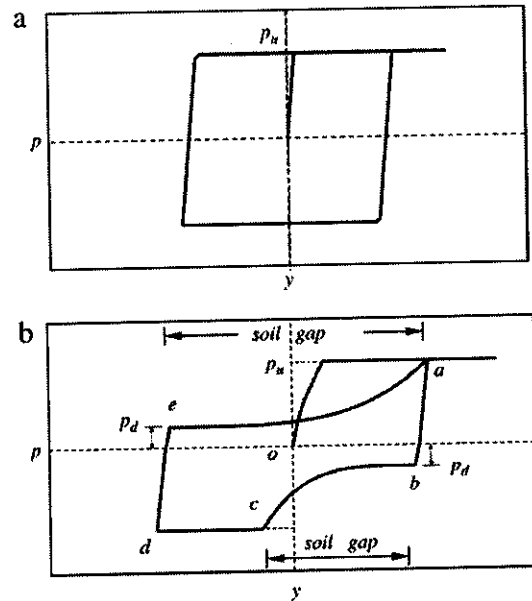


Fig. 4. Hysteretic p - y models: (a) Elastic-perfectly plastic model; (b) Dragging-gapping model.

The soil is loaded first along the monotonic branch oa and then is elastically unloaded with the initial stiffness until it reaches the dragging strength at p_d at point b in Fig. 4(b). As unloading is reloading and reloading continues in the opposite direction, the soil moves through the gap until it reaches the monotonic envelope on the opposite side at point c . A sixth-order polynomial is used to connect points b and c to model the gap-closing process. The same scenario of the unloading-reloading process is repeated for the branch dea . The dragging force is activated only when the pile moves through the gap. The value of the dragging strength p_d is taken as 30% of the monotonic peak capacity p_u , as suggested by Hutchinson et al. [27].

4. Applications

Two applications were selected to investigate the model parameters, to show the model capabilities, and to discuss the importance of modeling the pile-soil sub-system. The first one is a purely numerical example used to test the relevance of several model parameters through a set of parametric studies. The second one considers the experimental results of a cyclic test on a RC pile/shaft system where the influence of the pile-soil interaction is deemed essential.

4.1. A single pile embedded in sand

The pile-soil system shown in Fig. 5 is used to investigate the effects of the model parameters on the system response. Thirty beam-column elements are used to model the pile-soil system. Such a refined mesh is used to ensure that the converged solution is reached. The model parameters investigated include the pile length, the pile diameter, and the pile and soil nonlinearities.

4.1.1. Pile length

In this section, the pile response is kept linear elastic and the p - y curves of Fig. 3 are used to represent the responses of the surrounding sand. The pile-length effects on the lateral behavior are investigated by keeping the pile diameter constant at 0.5 m and varying the pile length from 5 to 15 m. Consequently, the pile slenderness ratios (L/D) range from 10 to 30. The pile-length effects

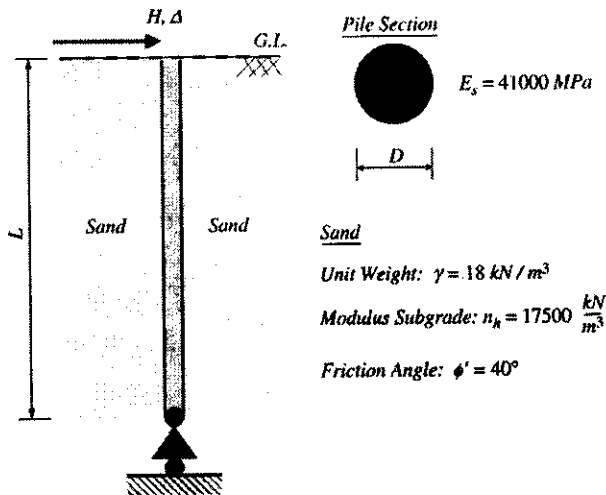


Fig. 5. Numerical example: An end-bearing pile embedded in sand.

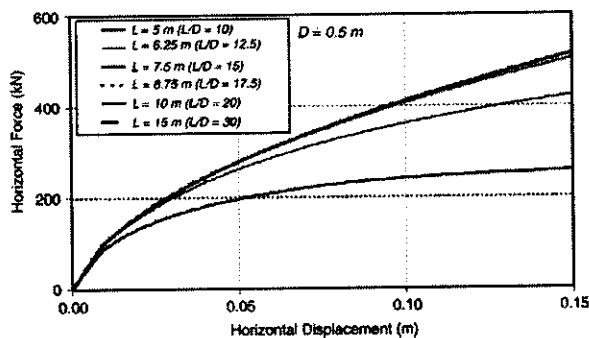
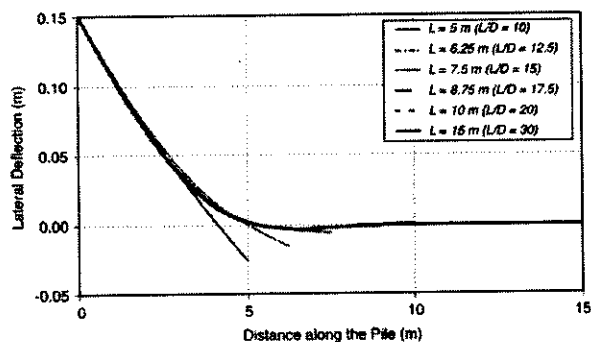


Fig. 6. Lateral load–displacement pile responses for different pile lengths.

Fig. 7. Deflected curves for different pile lengths (for a head displacement $\Delta = 0.15$ m).

on the global response are presented in the form of the lateral load–deflection curves in Fig. 6. The pile-length effects on the local responses are shown through the pile deflected shapes in Fig. 7 and the moment distributions along the pile in Fig. 8. These responses refer to a pile-head deflection of 0.15 m.

The pile length has little effect on the global response at the early loading stages. The explanation can be found by observing the pile deflected shapes in Fig. 7. Irrespective of the pile length, the top 3 m deform approximately the same way. The deflections of the rest of the pile, however, vary. The 5 m and 6.25 m long piles act as poles instead of piles. The tip deflections of the short pile are significant, hence resulting in yielding of the soils surrounding the pile tips. Conversely, the additional length of the longer pile acts as anchor and thus stiffens the pile.

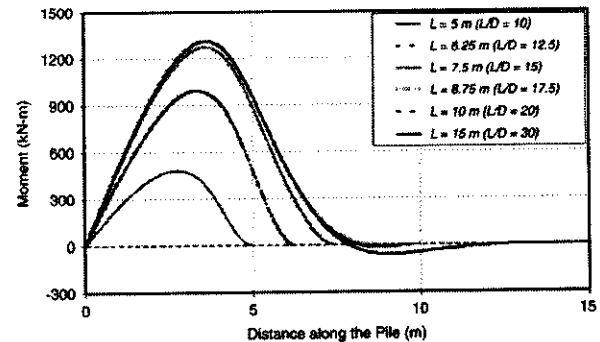
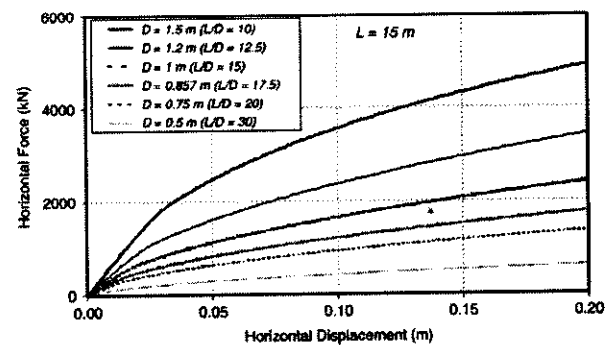
Fig. 8. Moment distributions along the pile for different pile lengths (for a head displacement $\Delta = 0.15$ m).

Fig. 9. Lateral load–displacement pile responses for different pile diameters.

Additionally, it can be observed that both global and local responses converge when the pile length is larger than 7.5 m ($L/D = 15$). In other words, the pile development length is approximately 7.5 m. This phenomenon is similar to the development length of the reinforcing steel in RC structural elements. For an elastic pile embedded in an elastic cohesionless soil, the characteristic length of the elastic soil–pile system is $\sqrt[3]{EI/n_h} = 4.72$ m [28]. This value is smaller than the observed development length of 7.5 m due to the fact that the characteristic length increases when the soil becomes nonlinear. It is observed in Fig. 8 that the maximum bending moment location is approximately the same for different pile lengths.

4.1.2. Pile diameter

In this section, the pile response is still kept linear elastic and the p – y curves of Fig. 3 are used to represent the response of the surrounding sand. The pile-diameter effects on the lateral behavior are assessed by keeping the pile length constant at 15 m and varying the pile diameter from 0.5 to 1.5 m. Consequently, the pile slenderness ratio (L/D) varies between 10 and 30. The pile-diameter effects on the global responses are presented in the form of the lateral load–deflection curves in Fig. 9. The pile-diameter effects on the local responses are shown by the pile deflected shapes in Fig. 10 and by the moment distributions along the pile in Fig. 11. These local responses are associated with the pile-head deflection of 0.20 m. Compared to the lateral responses in Fig. 9, it is observed that both lateral strength and stiffness of the pile–soil system continuously increase with larger pile diameter. It can also be noted that there is no converged response. This happens because enlarging the pile diameter results in a delayed sand yielding and in an increased lateral sand strength. This feature is taken into account in the p – y sand model of Fig. 3. Also, larger pile-diameters increase the pile–soil system stiffness.

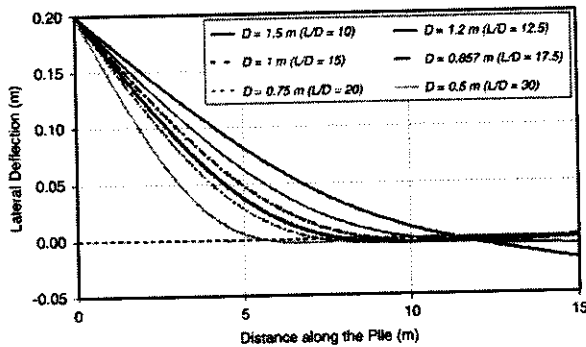


Fig. 10. Deflected curves for different pile diameters (for a head displacement $\Delta = 0.20$ m).

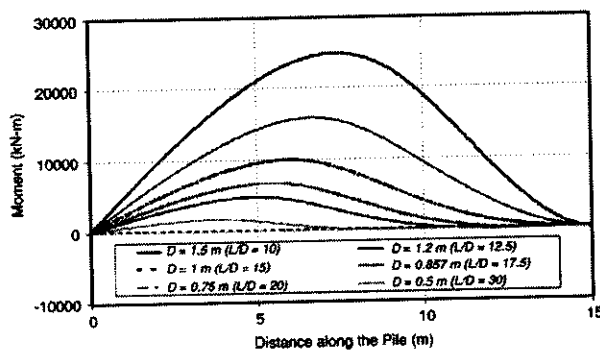


Fig. 11. Moment distributions along the pile for different pile diameters (for a head displacement $\Delta = 0.20$ m).

Similarly, there are no converged local responses found in Figs. 10 and 11. Furthermore, it should be noted that the system changes from pole to pile with increasing pile slenderness ratios (reduced pile-diameters). It is observed in Fig. 11 that the maximum-moment location gets deeper in the soil as the pile diameter increases. The increase in pile diameter results in mobilizing a greater soil depth.

4.1.3. Soil and pile nonlinearities

In this section, the RC pile embedded in sand of Fig. 12 is used to investigate the effects of soil and pile nonlinearities on the global and local system responses. This can be accomplished by analyzing and comparing the following four combinations: (a) Elastic-Pile/Elastic-Soil; (b) Elastic-Pile/Inelastic-Soil; (c) Inelastic-Pile/Elastic-Soil; (d) Inelastic-Pile/Inelastic-Soil. The aforementioned fiber-section model is used to represent the sectional responses of the RC pile. The fiber discretization of the RC pile section is shown in Fig. 12. The fiber section consists of

Concrete
 Confined Concrete: $f'_c = 45.4$ MPa
 Unconfined Concrete: $f'_c = 40.0$ MPa

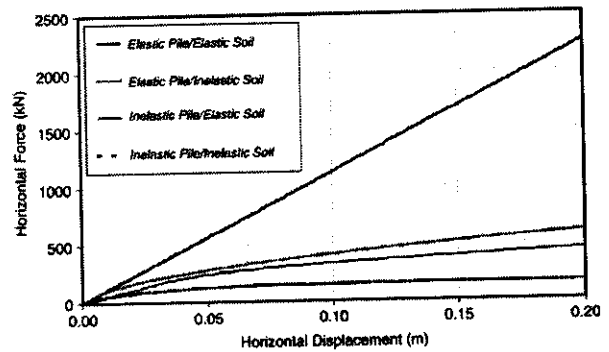
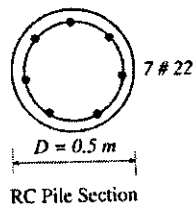


Fig. 13. Lateral load–displacement responses for different pile–soil systems.

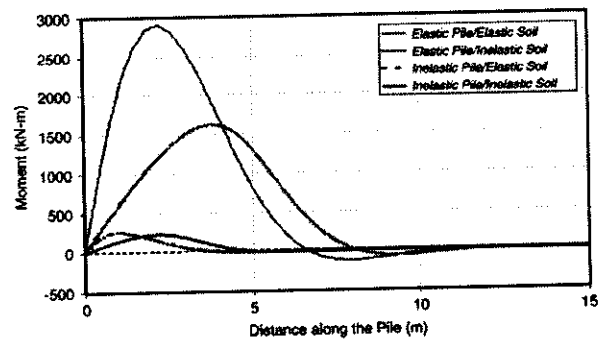


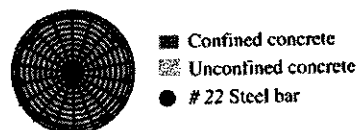
Fig. 14. Moment distributions along the pile for different pile–soil systems (for a head displacement $\Delta = 0.20$ m).

180 confined concrete fibers, 36 unconfined concrete fibers, and 7 steel fibers. Using the labeling of Fig. 12, the material properties are $f_y = 421$ MPa for the longitudinal reinforcement yield stress; $f'_c = 40$ MPa for the unconfined concrete strength; and $f'_c = 45.4$ MPa for the confined concrete strength.

The global responses of the four different pile–soil systems are shown in Fig. 13. Clearly, the soil and pile nonlinearities dictate the global response of the systems. The elastic system results in significantly larger stiffness and strength. Consequently, the soil and pile nonlinearities become essential when the performance-based methodology is employed in seismic design of structures.

The moment and curvature distributions along the pile length are shown in Figs. 14 and 15, respectively. Since the displacement-based model is employed in this study, there are discontinuities in the curvature and moment distributions between adjacent elements, because neither compatibility nor equilibrium is enforced between the two end sections of two adjacent elements. It is worth pointing out that the Gauss–Lobatto integration scheme is used in the element implementation, thus each of the two beam elements sharing a node has a monitored

Steel
 Yield Strength: $f_y = 421$ MPa
 Elastic Modulus: $E_s = 190500$ MPa



Fiber Section Discretization

Fig. 12. Fiber-section discretization of RC pile section.

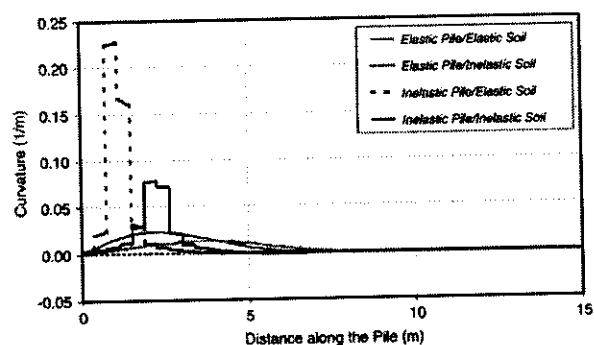


Fig. 15. Curvature distributions along the pile for different pile-soil systems (for a head displacement $\Delta = 0.20$ m).

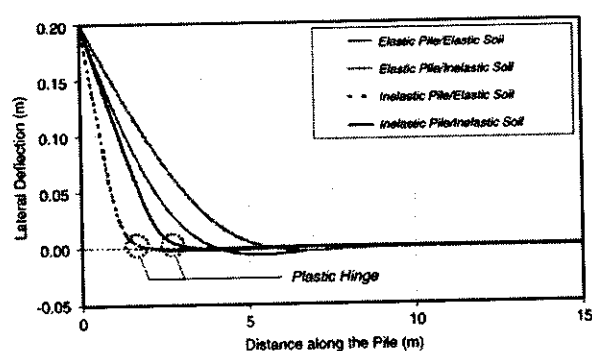


Fig. 16. Deflected shapes for different pile-soil systems (for a head displacement $\Delta = 0.20$ m).

section located at the nodal coordinates. The jump in the moment distribution between adjacent elements is rather small in Fig. 14 and is not clearly visible. Fig. 15 shows high curvature values that are consistent with those measured experimentally by Chai and Hutchinson [29,30]. In this particular case, a strain-hardening response is observed at the section level, thus no strain localization is to be expected. However, in other cases with a strain-softening section response the prediction could become mesh-dependent and the mesh should be carefully selected.

The local responses shown in Figs. 14 and 15 are associated with a pile-head deflection of 0.20 m. It is interesting to observe that the depth-to-maximum-moment ratio is larger when the soil nonlinearity is considered. This is due to the fact that yielding of the surrounding soil near the ground surface allows redistributions of the internal forces in a pile, thus shifting down the maximum-moment position. The pile-soil system is internally statically indeterminate; hence redistribution of internal forces is possible. The curvature distributions shown in Fig. 15 indicate that neglecting the soil nonlinearity results in over-predicting the curvature demand on the pile. This is due to the localization of the plastic hinge formed in the pile embedded in the elastic soil. The linear-elastic soil delays spreading of the plastic hinge, hence resulting in a shorter plastic-hinge length. This results in overestimating the local ductility demand on the pile.

Fig. 16 shows the deflected shapes of the piles for the different pile-soil systems. This local response is associated with a pile-head deflection of 0.20 m. It is observed that longer pile lengths are deformed when the soil nonlinearity is included. This is because longer pile lengths need to be mobilized in order to redistribute the internal forces in the system. The sections with higher curvatures in Fig. 16 indicate the location of the plastic hinge.

Fig. 17 shows the soil-force distributions along the pile for the different pile-soil systems. This local response is associated

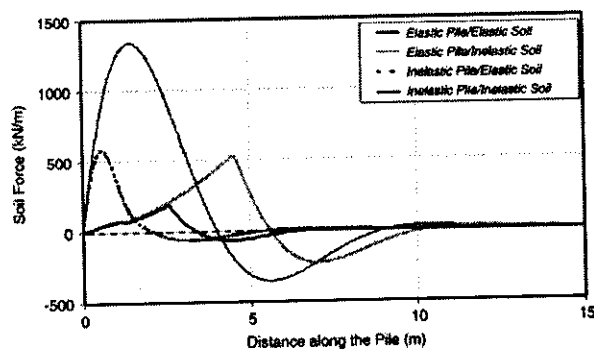


Fig. 17. Soil-force distributions along the pile for different pile-soil systems (for a head displacement $\Delta = 0.20$ m).

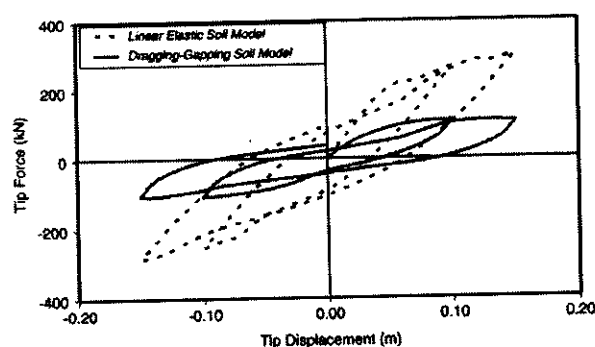


Fig. 18. Cyclic responses of soil-pile systems with elastic and dragging-gapping models.

with a pile-head deflection of 0.20 m. The trend in the soil-force distribution along the pile is only dictated by the soil response. Taking into account the soil nonlinearity results in a deeper location of the maximum soil force. Taking into account the pile nonlinearity results in a shallower maximum soil-force location. It is worth reminding that the soil strength is depth-dependent.

Fig. 18 compares the global responses of the pile embedded in the elastic soil with the pile embedded in the dragging-gapping soil. It is clear that the elastic soil model over-predicts not only the lateral strength of the system but also the hysteretic energy dissipated. However, the amount of hysteretic energy overestimated by the elastic soil model is not very large because the hysteretic energy can be dissipated only through the plastic hinge of the pile embedded in the elastic soil.

4.2. Chai-Hutchinson pile #1

Chai and Hutchinson [29,30] tested four RC piles embedded in sand under constant axial compression and reversed cyclic lateral displacements. These four piles representative of the Caltrans [31] design for 70 ton piles varied in confining reinforcement ratio, above-ground height, and sand density. In this paper, one of the experimental tests is used to evaluate the validity of the proposed beam-column model. This pile is labeled Chai-Hutchinson Specimen #1.

The geometry of this specimen is shown in Fig. 19. The pile was subjected to a constant axial compression of 489 kN (corresponding to approximately $f'_c A_g$) and the cyclic lateral tip-displacement history shown in Fig. 20. The longitudinal reinforcement for the pile section consists of 7 Grade A706 # 22 bars (diameter = 22 mm) corresponding to a longitudinal reinforcement ratio $\rho_l = 2.1\%$. The transverse reinforcement for the pile was provided by a continuous spiral of MW25 smooth wire

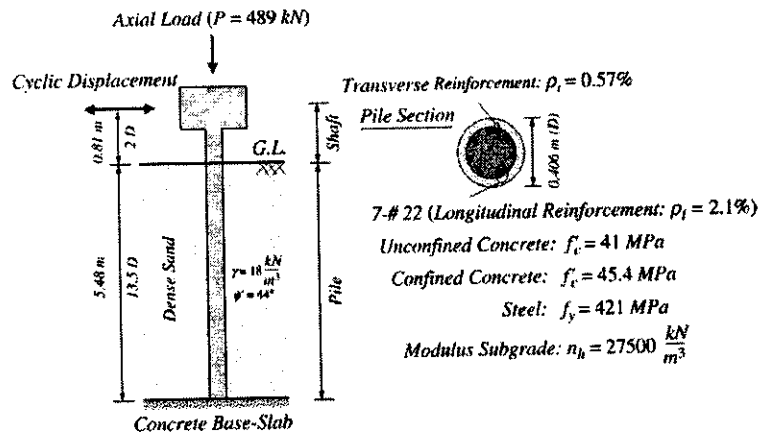


Fig. 19. Geometry and loads of Chai–Hutchinson [29,30] specimen #1.

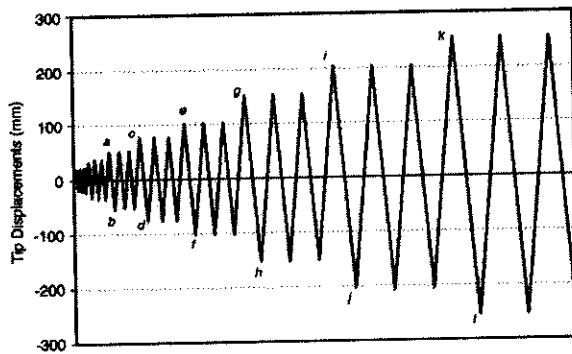


Fig. 20. Tip-displacement history of Chai–Hutchinson [29,30] specimen #1.

(diameter = 5.4 mm) at a 50 mm pitch. This amount of transverse reinforcement corresponds to a transverse reinforcement ratio $\rho_t = 0.57\%$, approximately one half of that required by ATC-32 [31]. Following Chai and Hutchinson [29,30] and using the labeling of Fig. 19, the material properties are $f_y = 421 \text{ MPa}$ for the longitudinal reinforcement yield stress; $f'_c = 41 \text{ MPa}$ for the unconfined concrete strength; and $f'_c = 45.4 \text{ MPa}$ for the confined concrete strength. As shown in Fig. 19, the surrounding sand has effective internal friction angle $\phi' = 44^\circ$; effective unit weight $\gamma = 18 \text{ kN/m}^3$; and modulus of horizontal subgrade reaction $n_h = 27500 \text{ kN/m}^3$ (as recommended by ATC-32 [32]). In the numerical model, the pile is discretized into 25 elements, plus 15 elements representing the shaft. The effects of the geometric nonlinearity on the system responses are also considered in the numerical model by including the $P-\Delta$ effects. This simplified treatment of the nonlinear geometric effects can be found in Filippou and Fenves [33]. The fiber-section discretization scheme of Fig. 12 is used to represent the section responses of the RC pile.

Fig. 21(a) superimposes the tip load–displacement experimental response with the numerical simulations obtained with the proposed model without dragging–gapping effects, while Fig. 21(b) compares experimental and simulated results obtained with the model with dragging–gapping effects. As expected, both models yield the same pile–soil strength, since the ultimate soil pressures of both models are computed based on Eq. (25) or (26). Neglecting the dragging–gapping effects can result in over-prediction of the hysteretic energy of the system. The model with the dragging–gapping effects can reproduce the initial stiffness and the peak lateral load, which is essential for the overall strength of the structural system. Furthermore, the model with the dragging–gapping effects can also reproduce the hysteretic cyclic

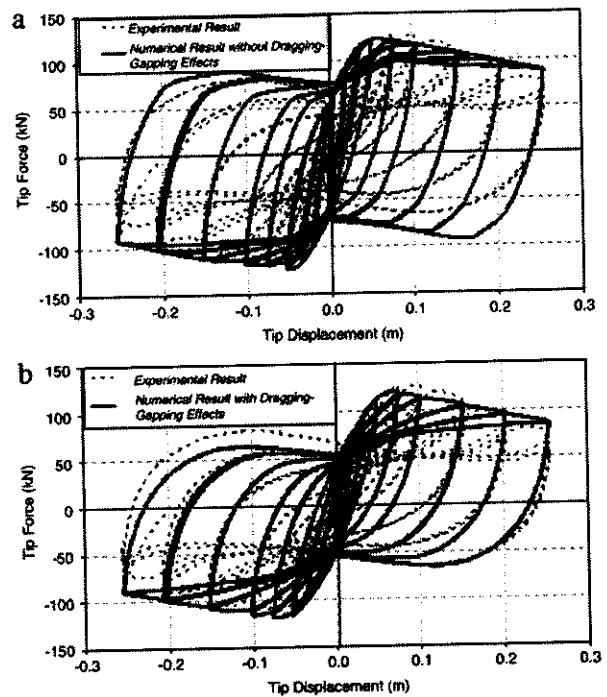


Fig. 21. Experimental and numerical responses of Chai–Hutchinson [29,30] specimen #1: (a) Model without dragging–gapping; (b) Model with dragging–gapping.

features of the system such as the unloading–reloading branches and the post-peak strength degradation.

Fig. 22 shows the lateral-displacement profiles of the pile at different loading cycles (the cycle numbers refer to the labeling of Fig. 20). Clear changes in the slope of the displacement profiles are observed. These are associated with the plastic-hinge formation, especially for large displacement cycles. The lateral deflections are rather small beyond the plastic-hinge region, implying that the inelastic pile deformations localize only within a depth of few pile diameters. When comparing the left (Fig. 22(a)) and right (Fig. 22(b)) deflection profiles, one can observe the distinct features of these two deflection directions. The gap formation along the left deflection tends to be larger than that along the right deflection. This behavior was also observed during the field tests by Chai and Hutchinson [29,30]. This non-symmetrical behavior was not captured when the dragging–gapping effects were not included in the numerical model.

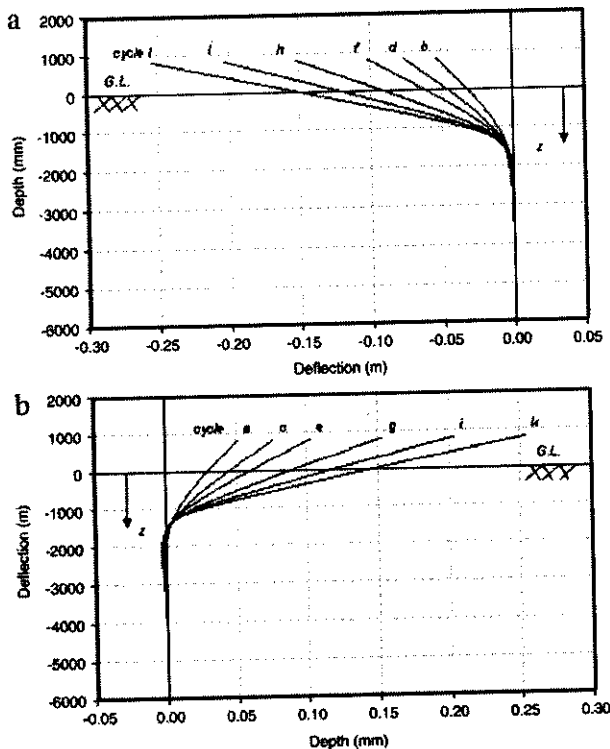


Fig. 22. Lateral-displacement profiles at different displacement cycles. (a) Left deflection; (b) Right deflection.

Fig. 23(a) and (b) show the pile moment and curvature profiles at different load cycles (the cycle numbers refer to the labeling of Fig. 20). As shown in Fig. 23, the depth-to-maximum-moment ratio (which indicates the plastic-hinge location) obtained with the proposed model is 1.25 m (3.08D). This value is in good agreement with the test observations of maximum damage to the pile at 1.09 m (2.69D) [29,30].

Fig. 24 shows the soil local responses at various depths. Fig. 24(a) shows the responses obtained with the elastic-perfectly plastic model (Fig. 4(a)) while Fig. 24(b) shows the responses obtained with the dragging-gapping model (Fig. 4(b)). As the depth increases, the maximum lateral pressure also increases but the maximum displacement decreases. This behavior is due to the p - y model used. These local responses further indicate that the dragging and gapping effects should be considered in order to correctly account for the cyclic soil-pile interaction.

The importance of the nonlinear geometric nonlinearities on the structural response was also investigated. The P - Δ effects are included in the numerical model of Fig. 21(b). Fig. 25 shows the same simulation, but the P - Δ effects are neglected. Although the shaft height (2D) of the Chai-Hutchinson Specimen #1 (Fig. 19) is relatively short, the P - Δ effect plays a crucial role in predicting the strength of the pile/shaft system due to the flexibility of the shaft base and the relatively high displacements applied. On the other hand, the P - Δ effects have a small influence on the system hysteretic energy.

5. Summary and conclusions

This paper presents a fiber beam-column model for a pile element that explicitly accounts for the interaction between the pile and the surrounding soil. The beam-column formulation is displacement based and leads to relatively simple and readily implemented equations. Material nonlinearities are included in the

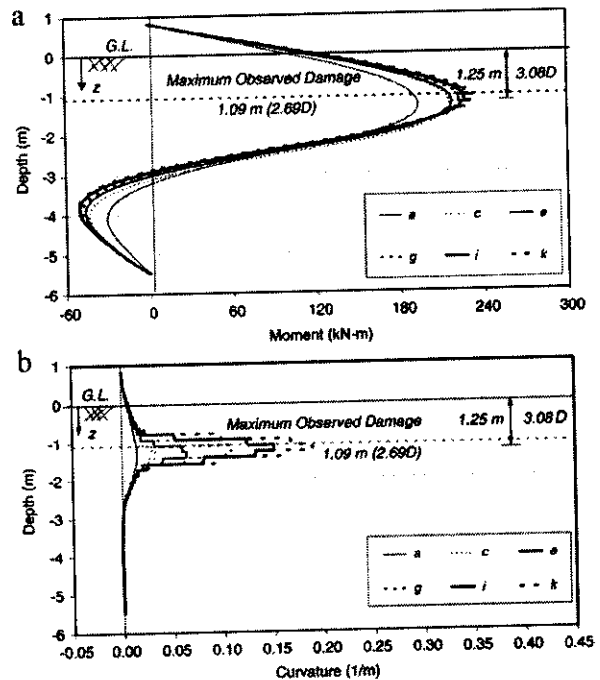


Fig. 23. Local response profiles at different displacement cycles: (a) Moment; (b) Curvature.

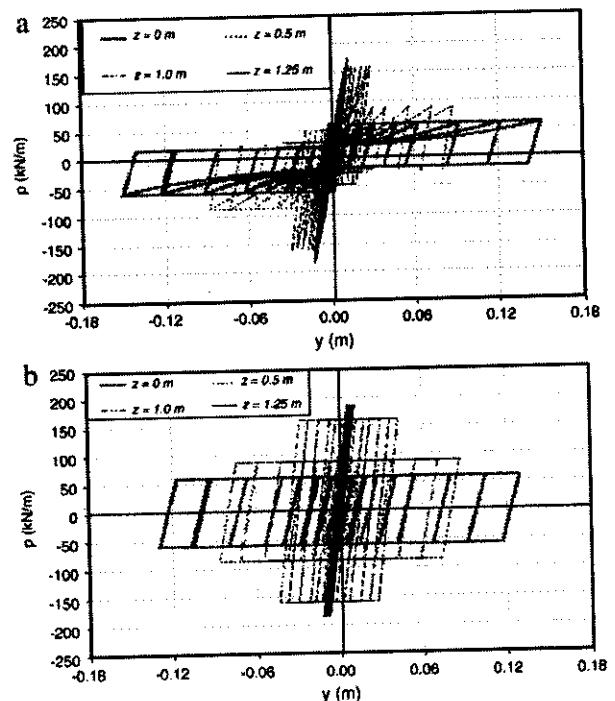


Fig. 24. Cyclic p - y responses at different depths: (a) Elastic-perfectly plastic model; (b) Dragging-gapping model.

uniaxial hysteretic laws for concrete, steel and surrounding soils. The so-called "Winkler Foundation" is employed to represent the soil in the form of p - y curves. The proposed p - y model can account for the dragging force and the gap formation along the pile-soil interfaces as well as the soil plasticity.

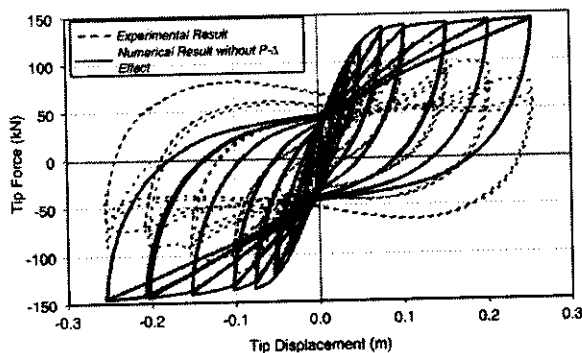


Fig. 25. Experimental and numerical responses of Chai–Hutchinson [29,30] specimen #1 without $P-\Delta$ effects.

The main scope of this work is to investigate the importance of different model parameters, to show the model capabilities, and to discuss the importance of modeling the pile–soil system when the pile head undergoes large lateral displacements.

In the first application, parametric studies on an end-bearing pile embedded in sand are used to investigate the effects of several model parameters (e.g. pile length, pile diameter, and pile/soil nonlinearities) on the lateral response of the pile–soil system. A summary of the findings follows:

Pile length: The pile length affects both global and local responses of the pile–soil system until a characteristic or development pile length. Beyond this pile length, the responses converge and the additional portions of the longer piles remain basically unloaded. The position of the maximum moment is approximately the same for different pile lengths. For relatively short piles, the system response is that of a pole rather than a pile.

Pile diameter: The pile diameter influences both global and local responses of the pile–soil systems. Both lateral strengths and stiffness of the pile–soil systems continuously increase with larger pile diameters. The maximum-moment positions are significantly affected by the pile-diameters. The maximum-moment location gets deeper in the soil as the pile diameter increases because larger pile diameters mobilize a greater soil depth.

Pile and soil nonlinearities: The soil and pile nonlinearities are essential, particularly when performance-based procedures are employed in seismic design of structures. The curvature demand is significantly over-predicted when the soil nonlinearity is neglected. The plastic-hinge location is deeper when the soil and/or pile nonlinearities are considered. Consequently, including the soil and pile nonlinearities in the analytical model can lead to a better design and avoid costly post-earthquake repairs.

The second application deals with the correlation studies on a large-scale test of a RC pile/shaft system under a constant axial compression and cyclic lateral tip displacements. The correlation studies indicate that the proposed model is capable of predicting well both the global and local responses of the pile–soil system despite the use of rather simple 1D $p-y$ springs to represent the surrounding soil. Neglecting the dragging and gapping effects results in the overestimation of the hysteretic energy and of the unloading–reloading stiffness of the pile–soil system. This feature is essential when the pile response under earthquake excitation is of interest. Although the shaft height (2D) is relatively short in the test; it is important to include the $P-\Delta$ effects for a correct prediction of the pile/shaft system response because of the flexibility of the shaft base and the relatively large displacements applied.

The two applications showed the characteristics and validity of the proposed model. This research will continue with the development of a soil–foundation–structure system for modeling

the response of bridges and buildings subjected to ground motions. Modeling the complete system may be important for large structures with foundations on softer soils, where the flexibility of the foundation–soil sub-system greatly affects the overall seismic response.

Acknowledgements

This study was partially supported by the Thai Ministry of University Affairs (MUA), by the Thailand Research Fund (TRF) under Grant MRG4680109, by the National Science Foundation under Grant No. CMS-0010112 and by the Italian Ministry of Education, University and Research (MIUR) under Cofin 2002 and 2004 Grants. These supports are gratefully acknowledged. Any opinions expressed in this paper are those of the authors and do not reflect the views of the sponsoring agencies. The authors would also like to thank Prof. Y.H. Chai of the University of California, Davis and Prof. T.C. Hutchinson of the University of California, San Diego for providing the experimental data used in this paper. Special thanks goes to Dr. Passagorn Chaiviriyawong for his fruitful input on the theoretical aspects. In addition, the authors would also like to thank three anonymous reviewers for their valuable and constructive comments.

References

- [1] NEHRP. Recommended provisions for seismic regulations for new buildings. Washington DC: Federal Emergency Management Agency; 1997.
- [2] Ghobarah A. Performance-based design in earthquake engineering: State of development. *Eng Struct* 2001;23:878–84.
- [3] Xue Q, Chen CC. Performance-based seismic design of structures: A direct displacement-based approach. *Eng Struct* 2003;25:1803–13.
- [4] Seed RB, Dickenson SE, Riemer MF, Bray JD, Sitar N, Mitchell JK, et al. Preliminary report on the principal geotechnical aspects of the October 17, 1989 Loma Prieta Earthquake. UCB/EERC-90/05. Berkeley: Earthquake Engineering Research Center, University of California; 1990.
- [5] Sitar N. Geotechnical reconnaissance of the effects of the January 17, 1995 Hyogoken-Nambu Earthquake, Japan. UCB/EERC-95/01. Berkeley: Earthquake Engineering Research Center, University of California; 1995.
- [6] Scawthorn C, Yanev PI. Preliminary report 17 January 1995, Hyogoken-Nambu, Japanese earthquake. *Eng Struct* 1995;17(3):146–57.
- [7] Mindlin RD. Force at a point in the interior of a semi-infinite solid. *Physics* 1936;7:195–202.
- [8] Desai CS, Appel GC. 3-D analysis of laterally loaded structures. In: 2nd international conference on numerical methods in geomechanics. Blacksburg: ASCE; 1976.
- [9] Kuhlmeier RL. Static and dynamic laterally loaded floating piles. *J Geotech Eng ASCE* 1979;105(2):289–304.
- [10] Winnicki LA, Zienkiewicz OC. Plastic (or visco-plastic) behavior of axisymmetric bodies subjected to non-symmetric loading—semi-analytical finite element solution. *Internat J Numer Methods Eng* 1979;14:1399–412.
- [11] Cai YX, Gould PL, Desai CS. Nonlinear analysis of 3D seismic interaction of soil–pile–structure systems and application. *Eng Struct* 2000;22:191–9.
- [12] Yang Z, Jeremic B. Numerical analysis of pile behavior under lateral loads in layered elastic-plastic soils. *Int J Numer Anal Methods Geomech* 2002;26(14):1385–406.
- [13] Budek AM, Priestley MJN, Benzoni G. Inelastic seismic response of bridge drilled-shaft RC pile/columns. *J Struct Eng ASCE* 2000;126(4):510–7.
- [14] Hoiit MI, McVay M, Hays C, Andrade PW. Nonlinear pile foundation analysis using Florida-Pier. *J Bridge Eng ASCE* 1996;1(4):135–42.
- [15] Alemdar BN, Güllkan P. Beams on generalized foundations: Supplementary element matrices. *Eng Struct* 1997;19(11):910–20.
- [16] Limkatanyu S, Spacone E. Frame element with lateral deformable supports: Formulations and numerical validation. *Comput Struct* 2006;84(13–14):942–54.
- [17] Küçükarslan S, Banerjee PK, Bildik N. Inelastic analysis of pile soil structure interaction. *Eng Struct* 2003;25:1231–9.
- [18] Winkler E. Theory of elasticity and strength. Prague: Dominicus; 1867.
- [19] Kent DC, Park R. Flexural members with confined concrete. *J Struct Div ASCE* 1971;97(7):1964–90.
- [20] Menegotto M, Pinto PE. Method of analysis for cyclically loaded reinforced concrete plane frames including changes in geometry and inelastic behavior of elements under combined normal force and bending. In: IABSE Symposium on resistance and ultimate deformability of structures acted on by well-defined repeated loads: Final report. 1973.
- [21] Taylor RL. FEAP: A Finite Element Analysis Program. User manual: Version 7.3. Berkeley: Department of Civil and Environmental Engineering, University of California; 2000.
- [22] Reese LC, Cox WR, Koop FD. Analysis of laterally loaded piles in sand. In: Proceedings of the annual offshore technology conference. 1974.